WARWICK
THE UNIVERSITY OF WARWICK

Manuscript version: Author's Accepted Manuscript
The version presented in WRAP is the author's accepted manuscript and may differ from the published version or Version of Record.

Persistent WRAP URL:
http://wrap.warwick.ac.uk/129255

How to cite:
Please refer to published version for the most recent bibliographic citation information. If a published version is known of, the repository item page linked to above, will contain details on accessing it.

Copyright and reuse:
The Warwick Research Archive Portal (WRAP) makes this work by researchers of the University of Warwick available open access under the following conditions.

Copyright © and all moral rights to the version of the paper presented here belong to the individual author(s) and/or other copyright owners. To the extent reasonable and practicable the material made available in WRAP has been checked for eligibility before being made available.

Copies of full items can be used for personal research or study, educational, or not-for-profit purposes without prior permission or charge. Provided that the authors, title and full bibliographic details are credited, a hyperlink and/or URL is given for the original metadata page and the content is not changed in any way.

Publisher's statement:
Please refer to the repository item page, publisher's statement section, for further information.

For more information, please contact the WRAP Team at: wrap@warwick.ac.uk.

warwick.ac.uk/lib-publications

Nanoscale Visualization and Multiscale Electrochemical Analysis of Conductive Polymer Electrodes

Enrico Daviddi,[1‡] *Zhiting Chen,*[2‡] *Brooke B. Massani,*[3] *Jaemin Lee,*[1] *Cameron L. Bentley,*[1*] *Patrick R. Unwin,*[1*] *and Erin L. Ratcliff*[2*]

[1] Department of Chemistry, University of Warwick, Coventry CV4 7AL, U.K.
[2] Department of Materials Science and Engineering, University of Arizona, Tucson, AZ USA
[3] Department of Chemistry and Biochemistry, University of Arizona, Tucson, AZ USA

ABSTRACT. Conductive polymers are exceptionally promising for application in modular electrochemical technologies including chemical sensors, bioelectronics, redox-flow batteries, and photo-electrochemical systems due to considerable synthetic tunability and ease of processing. Despite well-established structural heterogeneity in these systems, conventional macroscopic electroanalytical methods – specifically cyclic voltammetry – are typically used as the primary tool for structure-property elucidation. This work presents an alternative correlative multi-microscopy strategy; data from laboratory and synchrotron-based micro-spectroscopies, including conducting-atomic force microscopy and synchrotron nanoscale infrared spectroscopy, is combined with potentiodynamic movies of electrochemical fluxes from scanning electrochemical cell microscopy (SECCM) to reveal the relationship between electrode structure and activity. A model conductive polymer electrode system of tailored heterogeneity is investigated, consisting of phase-segregated domains of poly(3-

hexylthiophene) (P3HT) surrounded by contiguous regions of insulating poly(methyl methacrylate) (PMMA), representing an ultramicroelectrode array. Isolated domains of P3HT are shown to retain bulk-like chemical and electronic structure when blended with PMMA, and possess approximately equivalent electron-transfer rate constants compared to pure P3HT electrodes. The nanoscale electrochemical data are used to model and predict multiscale electrochemical behavior, revealing that macroscopic cyclic voltammograms should be much more kinetically facile than observed experimentally. This indicates that parasitic resistances rather than redox kinetics play a dominant role in macroscopic measurements in these conducting polymer systems. SECCM further demonstrates that the ambient degradation of the P3HT electroactivity within P3HT/PMMA blends is spatially heterogeneous. This work serves as a roadmap for benchmarking the quality of conductive polymer films as electrodes, emphasizing the importance of nanoscale electrochemical measurements in understanding macroscopic properties.

KEYWORDS: scanning electrochemical cell microscopy; SECCM; electrochemistry; electron transfer kinetics; P3HT; parasitic resistances; polymer degradation.

Conductive polymer electrodes have shown exceptional promise as active elements in next-generation energy harvesting and storage due to the ease of tuning the chemical, optical and electronic properties through synthesis. Additional favorable properties include mechanical flexibility, printability, biocompatibility and a hybrid electrical-ionic conduction mechanism, the latter of which has renewed interest in structure-property relationships of conductive polymer electrochemistry. A number of electrochemical devices and architectures have been developed, including organic bioelectronics,[1-3] thermogalvanics,[4] electrochromics,[5-7] supercapacitors,[8, 9] redox-flow batteries,[10] and photo-electrochemical devices.[11, 12] Recent advances in emergent wearable health-monitoring devices have inspired the inclusion of conductive polymers as sensing elements on fabrics and textiles, on the skin as electronic tattoos, and *in vivo*.[7, 13]

Yet one area less investigated is the use of organic electronic materials as electrochemically active elements in multi-electrode arrays, which can be coupled with chemical or optical assays for a number of molecular detection schemes. Arrays of ultramicroelectrodes (UMEs) necessitate isolated, electronically conductive domains on the order of microns to nanometers surrounded by a contiguous insulating material. Fabrication of UME arrays using conventional semiconductors is time and cost intensive and are often restricted to rigid substrates. Alternatively, the ease of printing polymeric materials enables thin film, planar structures that would serve to widen applications, especially in the life sciences.[14-16]

One over-arching challenge that remains is a more detailed understanding of the electrochemical behavior of printable conductive polymer electrodes. Conductive polymers follow a potential-dependent mechanism, whereby the kinetics of electron transfer are associated with the overlap in the density of states (DOS) of the electrode and electrolyte.[17] For semicrystalline polymers such as poly(3-hexylthiophene) (P3HT), the DOS is strongly connected to the microstructure, with crystalline domains being easier to oxidize than

amorphous regions.[18] The fraction of crystallites varies with processing and could hypothetically be altered when the conductive polymer is constrained into a UME configuration. Thus realization of all-organic electrochemical devices necessitates a detailed understanding of the nanoscale structure-property relationships governing charge transfer and how these relationships influence measurements on larger length scales.

Herein, the nanoscale electron-transfer kinetics of a model system has been considered: blends of a semi-crystalline conductive polymer, P3HT, and amorphous insulator poly(methyl methacrylate) (PMMA). P3HT was chosen as the model conductor for organic electrochemical systems as it is well-studied, both structurally and electrochemically (at the macroscale).[11, 19, 20] As the interest is on nanoscale behavior and connections to UME arrays, P3HT was blended with PMMA as the system is known to possess microstructural heterogeneity arising from phase segregation.[21, 22] Previously, P3HT/PMMA microstructural domains have been used to improve charge transport in organic field effect and electrochemical transistors, to obtain high transmittance while retaining conductivity in opto-electronics, and to alter photoluminescence.[21, 23-25] More broadly, blending a conductive polymer with a non-conjugated system is used to acquire new mechanical, optical, morphological and thermal properties, or to introduce strategic intermolecular forces for adhesion/binding, coulombic charge stabilization, or promote desired chemical-electrochemical reactions.[26]

Conventional macroscopic electroanalytical methods, notably cyclic voltammetry, are typically used as the main tool to study the properties of conductive polymer electrodes and compare behavior across materials sets to elucidate electrochemical structure-property relationships. As explored herein, the nanoscale spatial-heterogeneity arising from phase segregation in polymer blend electrodes can be addressed most powerfully using the local electrochemical technique scanning electrochemical cell microscopy (SECCM)[27,28] to fully understand the relationship between local chemical composition and electrochemical

reactivity.[29, 30] Indeed, this approach has been previously demonstrated with many classes of (electro)material, including: sp^2 carbon electrodes (*e.g.*, graphite, nanotubes and graphene),[31] battery materials,[32] electrocatalysts (*e.g.*, transition metal dichalcogenides,[33-35] iron nickel sulfides,[36] polycrystalline metals[37-39] etc.) and corroding metals.[40]

In this contribution, voltammetric movies from SECCM of the rapid outer-sphere electron transfer process $FcDM^{0/+}$ (where FcDM stands for 1,1′-ferrocenedimethanol) at complex, phase-separated P3HT/PMMA blend electrodes have been correlated with complementary, co-located high-resolution conductive atomic force microscopy (c-AFM) to reveal unambiguously electrical-electrochemical interconnections in the blends. Alternatively SECCM is relatively immune to such effects. With this added understanding, the ambient exposure-induced degradation of P3HT/PMMA blend electrodes is interrogated with SECCM, demonstrating a spatially heterogeneous loss in electrochemical redox behavior. These results emphasize the importance of nanoscale resolution in correlative electrochemical-structural measurements, revealing structural controls in the response of complex heterogeneous electrodes and explaining electrochemical behavior at the macroscale.

RESULTS AND DISCUSSION

The development of random arrays of UME discs comprised of the conductive polymer P3HT, where the insulating domains are formed by PMMA, was considered in this work. Initially, three blend ratios were fabricated: 5:1, 1:1, and 1:5 P3HT:PMMA in wt% (preparation and characterization are detailed in Methods Section and in the Supporting Information, Section S.1). Each of the three mixed polymer electrodes were characterized in terms of chemical and physical structure using c-AFM, x-ray photoelectron spectroscopy (XPS) and optical spectroscopy, summarized in brevity in Figure 1.

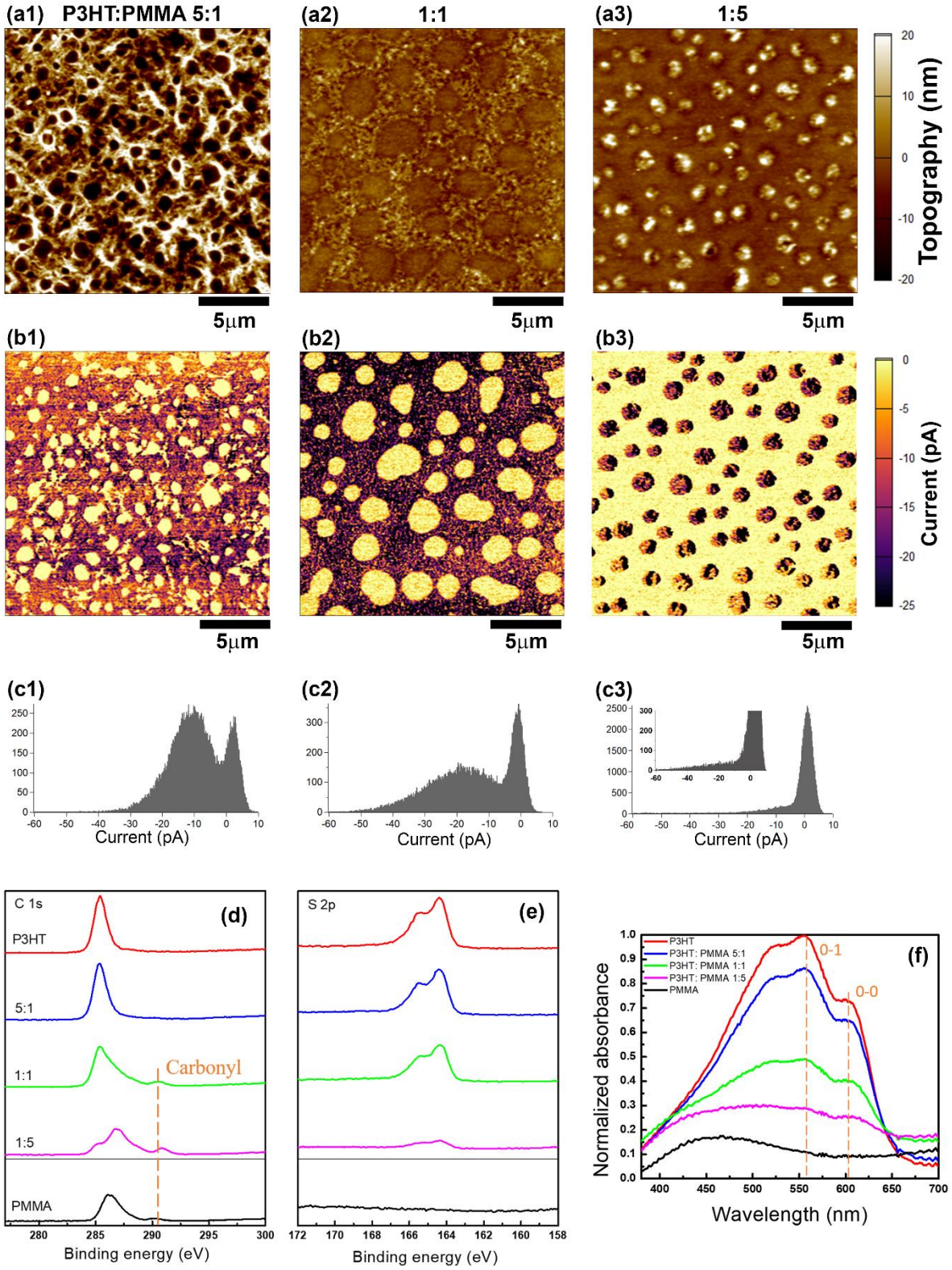

Figure 1. c-AFM of P3HT: PMMA **(a)** 5:1, **(b)** 1:1 and **(c)** 1:5 blended films on ITO glass substrates. All figures show the topographic image in row 1 **(a1 – a3)**, the conductance current in row 2 **(b1 – b3)** and conductance current distribution histogram in row 3 **(c1 – c3)**. Sample bias applied to achieve ~60pA maximum current for each film: -1.5V for the 5:1 film (b1 and c1), -0.5V for the 1:1 film (b2 and c2) and -2.5V for the 1:5 film (b3 and

c3). X-ray photoelectron spectroscopy spectra showing the core levels of the noted P3HT:PMMA blend ratios (marked on the figure), showing respectively the **(d)** C 1s peaks and **(e)** S 2p peaks. **(f)** UV-visible absorbance spectra of spin-coated thin films with different ratios of P3HT:PMMA. The inset in (c3) shows the distribution at an enhanced y-scale.

AFM tapping mode topography and current maps are shown in Figure 1a-b, respectively, while Figure 1c shows the relative conductance current distribution histogram for each of the three blends. All three blends presented two sub-populations at the nanoscale, as measured using c-AFM, with a strong connection between the areas of raised topography and local conductivity, attributed to P3HT domains. By contrast, the PMMA regions showed no current response at the pA limit. Both the 5:1 and 1:1 blend ratios yielded domains of PMMA surrounded by contiguously conductive P3HT (Figures 1b-1 and 1b2). Alternatively, the 1:5 blend produced randomly distributed µm-sized P3HT domains approximately 10-20 nm in height and 2 µm in diameter (Figure 1b-3), resulting in islands that yielded a conductance current of ≈ -25 pA under a negative 2.5V bias. Thus, the 1:5 blend ratio served as a model for UME arrays and is the major focus of this work.

Within this 1:5 P3HT:PMMA sample, there is a significant heterogeneity in electrical properties (*i.e.*, conductivity) both within segregated domains and between domains (Figures 1a,b,c-3). Origins of this heterogeneity in conductivity could be due to local differences in chemical structure (*i.e.*, vertical phase segregation and/or chemical reactions) and/or differences in microstructure of the P3HT. X-ray photoelectron spectroscopy (XPS) suggests a higher concentration of PMMA at the surface of the 1:5 blend ratio; only 9% of the surface chemical composition is P3HT, as determined by the integrated peak area ratio between the high binding energy C 1s carbonyl peak of the methacrylate (Figure 1d) and the thiophene S $2p_{3/2}$ peak (Figure 1e). This observation is consistent with the difference in surface energy between the two polymers and is supported by the c-AFM data. Using a tapping mode image with 5 nm height threshold, a P3HT surface coverage of 11 ± 2% was determined for square

areas of both 5 and 20 micron length (Figure S3-a3). A P3HT surface coverage of 11.5% was calculated by c-AFM image with -5 pA threshold, the result being consistent with that of height images (Figure 1 b3). No chemical interaction was observed between the P3HT and PMMA with XPS for any of the three blend ratios, relative to the neat polymer films. Additional ratios are provided in Table S1.

The opto-electronic properties of the blends were characterized using UV-visible absorbance, shown in Figure 1f, which demonstrates the trend in scaled absorbance with PMMA ratio. Microstructural changes were not observed optically using the exciton vibronic peak ratio of the 0-0 and 0-1 transition (Supporting Information, Table S2). Grazing incidence wide-angle x-ray scattering (GIWAXS) was performed on each sample to rule out changes in interchain packing of the semicrystalline regions of P3HT. 2D detector images and one dimensional-GIWAXS plots for a cake slice in the q_z (out-of-plane) and q_{xy} (in-plane) direction, with readily observable (100), (200), and (300) plane spacings are shown in the Supporting Information (Section S.2, Figures S4 and S5). In all cases, the common edge-on orientation of the P3HT crystallites was observed, with preservation of the lamellar and π-π- stacking distances (Table S3). Therefore, the heterogeneity observed in electrical properties in Figure 1b-c cannot be rationalized as changes in P3HT microstructure within the resolution of standard characterization techniques.

Synchrotron nanoscale infrared spectroscopy (SINS). As an addition, synchrotron infrared nanoscale spectroscopy (SINS) was used to investigate the possibility of vertical phase segregation and/or intercalation of PMMA into the P3HT domains. The results are shown in Figure 2. Briefly, SINS combines a broad spectrum of infrared light with an atomic-force microscope to characterize nanoscale chemical features.[51] The signal is generated from the portion of light scattered from the AFM tip that has experienced electromagnetic enhancement (near-field). In this configuration, only single point spectra can be acquired (*vide infra*). Figure

2a shows the AFM tip amplitude image of a small P3HT area surrounded by PMMA and specifies the location of 14 different points used to generate a line scan shown in the color map in Figure 2b. Full spectra are provided in the Supporting Information, Figure S6. The characterization was focused on the carbonyl region ($\bar{\nu}$ = 1734 cm^{-1}) for the PMMA, due to the strong molar absorptivity; P3HT is vibrationally silent in this region. For reference, the far-field spectra for the neat polymers (P3HT and PMMA) and the 1:5 P3HT:PMMA blend are shown in Figure 2c.

Figure 2b provides clear chemical verification that the topographically elevated domains are P3HT, surrounded by contiguous insulating PMMA, as evident by the strong intensity of the reported signal centered at 1734 cm^{-1} for positions 1-3 and 12-14 and minimal signal for positions 4-11. However, it should be noted that there is a non-zero signal (above the baseline) at points 4-11 suggests small fractions of PMMA are located within the P3HT domain. This observation is at the signal-to-noise limit, and the lack of vertical resolution limits distinction of whether PMMA is phase segregated at the top of the P3HT or buried near the ITO surface. However, the local electrochemical properties of the polymer could provide more insight into the electrical heterogeneity, as the redox behavior of the polymer electrode is correlated with the local DOS.

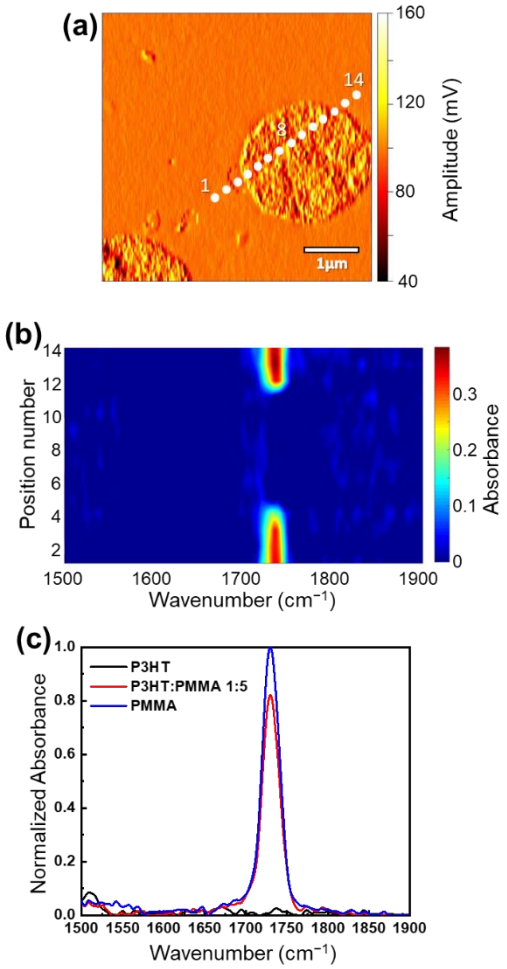

Figure 2. Synchrotron infrared nanoscale spectroscopy of P3HT domain in PMMA (sample was 1:5 P3HT PMMA) **(a)** Amplitude image of the line scan across P3HT island used to collect near-field infrared nanospectroscopy and **(b)** infrared spectra across the 14 identified positions in (a). The presence of peaks at 1734 cm^{-1} are the carbonyl stretch of the PMMA. **(c)** Far-field spectra of neat polymers (P3HT and PMMA) and 1:5 films.

Correlative electrochemical multi-microscopy for nanoscale kinetic analysis. The spatially-dependent electron-transfer characteristics of pure P3HT and 1:5 P3HT:PMMA blend films were probed at the nanoscale using SECCM.[27-29] In SECCM, local electrochemical measurements (*e.g.*, voltammetry,[41] amperometry[34] or potentiometry[42]) are performed within a confined area of a surface, defined by the dimensions of a droplet (meniscus) cell formed at the end of an electrolyte-filled nanopipet equipped with quasi-reference counter electrode(s) (QRCEs).[27, 28] The voltammetric hopping mode of operation was employed,[41] using a dual channeled nanopipet probe (diameter ≈ 100 − 200 nm, see Supporting Information, Figure S1),

filled with 4.5 mM FcDM and 100 mM KCl. The dual barrels were equipped with Ag/AgCl QRCEs which possess a stable potential of *ca.* 0.070 to 0.080 V (measured to 1 mV) vs Ag/AgCl (3.4 M KCl).[43] Note that unless otherwise stated, all potentials herein are corrected to the Ag/AgCl (3.4 M KCl) reference scale. During operation, a small potential bias (50 mV) was applied between the identical QRCEs located in the two channels of the probe, inducing a *dc* ion current ($i_{dc} \approx 250$ pA), which was used as a feedback signal for probe positioning (*i.e.*, to detect when meniscus contact had been made between the probe and the surface of interest). Note that this i_{dc} feedback is independent of the substrate conductivity and thus can be used to position the probe on both the P3HT (conductive) and PMMA (non-conductive) domains of the polymer blend electrode.[27, 44] Further details on the SECCM set up employed are available in the Methods Section.

SECCM was initially performed on freshly prepared films of P3HT and 1:5 P3HT:PMMA by performing cyclic voltammetry in the potential range *ca.* − 0.14 to 0.75 V vs Ag/AgCl (*i.e.*, − 0.2 to 0.6 V vs Ag/AgCl QRCE) to observe the $FcDM^{0/+}$ redox process. The $FcDM^{0/+}$ electron transfer reaction is a rapid, mechanistically simple, outer-sphere process on most conventional (*e.g.*, metal and carbon) electrode materials:[45]

$$FcDM \rightleftharpoons FcDM^{+} + e^{-} \quad (1)$$

As the nanopipet probes used in SECCM possess a conical geometry, mass-transport is predominantly governed by quasi-radial diffusion, resulting in relatively high rates of mass-transport that allow (near) steady-state conditions to be established on the voltammetric timescale explored herein (*i.e.*, ms timescale at voltammetric scan rate, $\upsilon = 1$ V s^{-1}).[46, 47] The heterogeneous electron-transfer rate constant (k^0) and transfer-coefficient (α) are calculated numerically from the experimentally derived formal ($E^{0'}$), half-wave ($E_{1/2}$) and quarter-wave ($E_{1/4}$ and $E_{3/4}$) potentials[48] (further details on the procedure can be found in the Supporting Information, Section S.4).

A spatially-resolved electrochemical flux movie for the $FcDM^{0/+}$ process on an area of the pure P3HT film electrode is shown in the Supporting Information, Movie S1. A single frame from the movie, obtained at a potential where $FcDM^{0/+}$ is mass-transport limited (*i.e.*, 0.65 V vs Ag/AgCl) is also shown in the Supporting Information, Figure S10a. Evident from Movie S1 and Figure S10a, the P3HT film exhibits relatively uniform electrochemical activity towards the $FcDM^{0/+}$ process throughout the entire potential range, with the exception of a few non-conductive areas of ≈ 2 μm size. Comparison with the synchronously obtained topographical (*z*-height) map (Figure S10b) reveals no correlation between the physical structure and electrochemical activity, with the film possessing a surface roughness on the same scale (*ca.* 15 nm RMS) as the underlying indium tin oxide (ITO) support.

For comparison with conventional electrodes (*i.e.*, metals), a classical Nernstian behavior and underlying Butler-Volmer mechanism was assumed; the limitations of these assumptions for conductive polymer electrodes have been detailed previously,[49] but regardless, provide an initial point of comparison. The uniform electrochemical activity of the P3HT film is reflected in the spatially-resolved k^0 map shown in Figure S10c, from which surface average (9567 individual measurements) values of $k^0 \approx 3 \times 10^{-2}$ cm s^{-1} and $\alpha \approx 0.6$ are derived (see below for the discussion about the statistical distributions of these values). Note that this k^0 value is orders-of-magnitude lower than that usually measured for the oxidation of ferrocene and derivatives at conventional metal or carbon electrodes, which are usually on the order of 1 - 10 cm s^{-1}.[45] This is expected based on the significantly lower intrinsic DOS of polymeric electrode materials (P3HT) compared to conventional metallic conductors. However, these average results are much larger than previously reported macroscale cyclic voltammetry measurements of the $FcDM^{0/+}$ process on electrodeposited P3HT ($k^0 \approx 7 \times 10^{-4}$ cm s^{-1}), which exhibited clear (electrochemical) irreversibility.[49]

As noted above, the 1:5 P3HT:PMMA blend electrode is structurally heterogeneous, with segregated P3HT and PMMA domains, as revealed from AFM imaging, and further illustrated in Figure 3a. Note that the c-AFM data in Figure 1 and 3 were obtained from two different 1:5 P3HT:PMMA blend electrodes and on different instruments in the USA and UK, respectively, highlighting the reproducibility of the electrodes. Furthermore, these c-AFM data are specifically presented for direct comparison with SECCM below. Probing the conductivity of the domains with c-AFM revealed the elevated islands (*ca.* 10 nm in height, Figure 3a) to be conductive P3HT domains (conductance current of *ca.* +10 pA above the non-conducting baseline, at +2 V), within a "sea" of insulating PMMA, shown in Figure 3b and consistent with Figure 1a,b-3. The individual P3HT/PMMA domains also contrast optically, as shown in Figure 3c. From Figure 3a-c, the roughly circular P3HT domains (islands) are on average *ca.* 2.3 μm in diameter and separated by an average distance of *ca.* 2.9 μm.

Voltammetric SECCM was carried out on the same scanned area using the protocol outlined above; the synchronously obtained topographical map is shown in Figure 3d. The morphology (*i.e.*, height, shape and diameter) of the individual P3HT domains in Figure 3d is qualitatively similar to the co-located AFM map in Figure 3a, demonstrating the high-fidelity of SECCM topographical mapping.[34] The corresponding spatially-resolved electrochemical flux movie for the $FcDM^{0/+}$ process on the blend electrode is shown in the Supporting Information, Movie S2. A single frame from the movie, obtained at a potential where the $FcDM^{0/+}$ process is mass-transport limited on the individual P3HT domains (*i.e.*, 0.74 V vs Ag/AgCl) is also shown in Figure 3e. Evident from Movie S2 and Figure 2e, the polymer blend electrode possesses highly heterogeneous electrochemical activity, with the P3HT domains (*i.e.*, red areas in Figure 3e) supporting the $FcDM^{0/+}$ process, while only non-faradaic current arising predominantly from stray capacitance (*ca.* 0.8 pA) was measured on the insulating PMMA domains (*i.e.*, blue areas in Figure 3e).

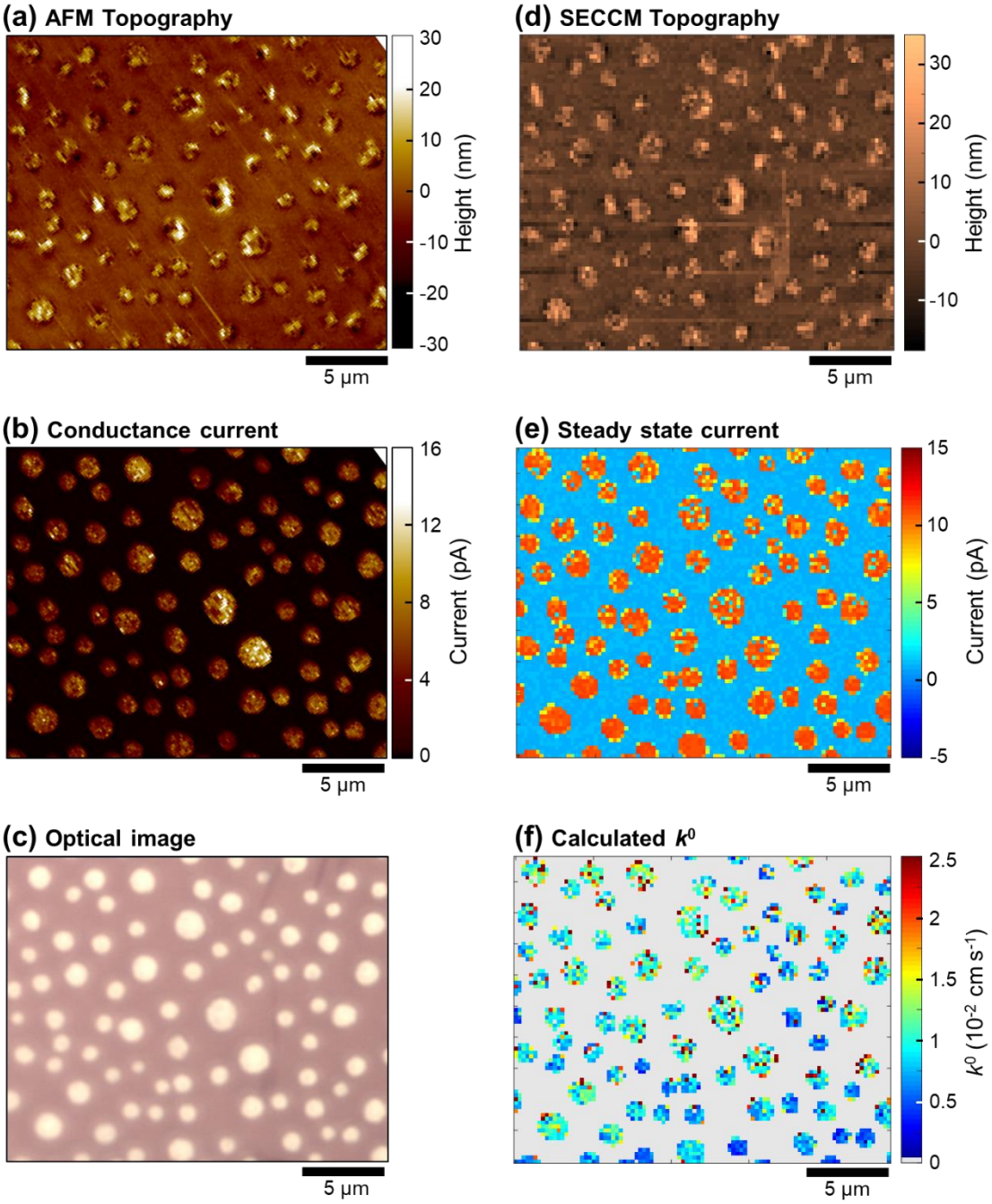

Figure 3. Correlative multi-microscopy analysis of the surface of a 1:5 P3HT:PMMA blend electrode, deposited on an ITO support. **(a)** Topographical and corresponding **(b)** electrical conductivity maps, measured using c-AFM (bias potential = +2.0 V). **(c)** Optical microscopy image (reflected light, 500× magnification). **(d)** Topographical and corresponding **(e)** synchronous electrochemical activity map recorded in the SECCM configuration (97 by 79 pixels, hopping distance = 0.25 µm, 2.85 s pixel^{-1}). (e) Single frame of Movie S2, taken at 0.74 V vs Ag/AgCl. **(f)** Map of k^0 values for the FcDM$^{0/+}$ process, calculated numerically from spatially-resolved i–E data from SECCM (Supporting Information, Movie S2). In (f), the color scheme was applied only where full steady-state voltammograms were measured (*i.e.*, on the P3HT domains); otherwise, it was assigned no color and coincides with the insulating PMMA domains. The nanopipet probe used for SECCM, (d – f), was ≈ 200 nm in diameter and contained 4.5 mM FcDM + 100 mM KCl.

Considering potentials where the $FcDM^{0/+}$ process is kinetically limited (*i.e.*, at $E < E_{1/2}$, *ca.* 0.2 to 0.4 V vs Ag/AgCl) in Movie S2, it is clear that the individual P3HT domains are not uniformly active. The larger domains on average show higher electrochemical activity (*i.e.*, higher currents at a given potential) than the smaller domains, explored further below. Upon sweeping to more positive potentials (*i.e.*, $E > 0.6$ V, Figure 3e), all P3HT domains attain a mass-transport limited current of *ca.* 11 pA. This limiting current is approximately 10% of what is expected at a conventional inlaid metal disc electrode of the same diameter as the used nanopipet probe (*ca.* 200 nm in Figure 3, see Figure S1), in agreement with theoretical predictions of SECCM mass transport.[47] Note that in Figure 3e, pixels located at the edges of the islands exhibit currents that are smaller than the mass-transport limit due to the co-contribution of conductive P3HT and non-conductive PMMA within the area probed by the meniscus cell (*i.e.*, only a fraction of the probed area is conductive/active).

Using the numerical approach outlined in the Supporting Information, Section S.4, pixel-resolved electrode kinetic parameters (*i.e.*, k^0 and α values) were extracted, as illustrated by the spatially-resolved k^0 map in Figure 3f. Considering all of the active P3HT domains (1826 individual measurements), average k^0 and α values of 8×10^{-3} cm s^{-1} and 0.4 were calculated, corresponding to a *ca.* 4-fold decrease in the $FcDM^{0/+}$ electrode kinetics compared to the pure P3HT case above (Supporting Information, Figure S10).

Evidently, the electrode kinetics associated with the $FcDM^{0/+}$ process is P3HT domain-dependent, with the intra-domain variation being smaller than the inter-domain variation. In general, the k^0 values measured on an individual P3HT domain (island) are relatively homogeneous and also tend to be larger on the largest islands (see Supporting Information, Figure S11b). Larger islands also coincide with the largest conductance currents in the solid state (see Figure S11a). This effect, as briefly discussed in the Supporting Information Section S.5 may be due to the geometry of the conducting and electrochemical probe arrangements,

but other effects between individual domains cannot be ruled out, including localized differences in sample thickness, small differences in domain composition, and spatial variations in potential and charge density distributions.[50]

Predicting the macroscopic voltammetric response of polymer blend electrodes. Steady-state voltammograms from the pure P3HT film and 1:5 P3HT:PMMA blend electrodes obtained by averaging all of the active "pixels" in Movie S1 and S2, respectively, are shown in Figure 4a. There is a relatively high mass-transport coefficient achieved in the SECCM configuration with the nanoscale probes[47] employed herein ($k_m \approx 8 \times 10^{-2}$ cm s^{-1}), estimated from the mass-transport-limited current calculation detailed in Supporting Information, Section S.4. Kinetically, both the pure P3HT film (red trace, $k^0 \approx 3 \times 10^{-2}$ cm s^{-1}) and 1:5 P3HT:PMMA polymer blend (green trace, $k^0 \approx 8 \times 10^{-3}$ cm s^{-1}) can be statistically distinguished from the other, as well as from the electrochemically reversible case (as measured on a nanocrystalline Au electrode, blue trace, $k^0 > 1$ cm s^{-1}).[45] The difference between the two polymer films can be attributed, in part, to the inclusion of a small fraction of PMMA within the P3HT domains, as determined from the SINS data in Figure 2. The numerically derived k^0 values for both the pure P3HT and 1:5 P3HT:PMMA electrodes both follow log-normal distributions, as shown in Figure 4b.

Log(k^0) is proportional to the standard free energy of activation for a heterogeneous electron-transfer reaction, which, in this case, will be composed of the reorganization energy and work terms (as per Marcus theory[52]), and the energetic barrier of the actual electron transfer event, which is dependent on the DOS and other parameters.[53] As $FcDM^{0/+}$ is a well-known outer sphere redox couple, the electron transfer rate is most likely to be limited by the relatively low DOS of P3HT (which is why the kinetics of $FcDM^{0/+}$ is measurable). Note that the apparent energy barriers observed (inferred from k^0) are averages over the area probed during each SECCM measurement (*e.g.*, Figure 2e and Movie S2), comprising a multitude of sites with

different properties (*e.g.*, local DOS). It is the distribution in electrochemical activities between these elementary sites of P3HT that gives rise to the log-normal distributions in Figure 3b. This also explains why the distributions in Figure 3b are of the same width (*i.e.*, standard deviation of 0.3 in both cases), as the electrode material (P3HT) and redox process ($FcDM^{0/+}$) under investigation are identical. This result is also consistent with the solid state structural characterizations of the P3HT and 1:5 P3HT:PMMA detailed in Figure 1 and Supporting Information, Section S.2 (*i.e.*, the P3HT is microstructurally analogous in both the pure film and the blend electrodes).

In order to predict the macroscopic electrochemical response from the nanoscale measurements for the three different electrodes considered, FEM simulations were conducted. The Au (k^0 = 1 cm s^{-1}, α = 0.5, essentially reversible) and pure P3HT film ($k^0 = 3 \times 10^{-2}$ cm s^{-1}, α = 0.6) cases were simulated assuming mass-transport occurred solely by planar (1D) diffusion to a homogeneously active electrode surface. The 1:5 P3HT:PMMA blend electrode case was simulated with a 2D axisymmetric geometry, shown in Figure 4c, where the central area represents a conductive P3HT domain ($k^0 = 8 \times 10^{-3}$ cm s^{-1}, α = 0.4) while the surrounding ring represents a non-conductive PMMA domain (set as a no flux boundary). The radius of the P3HT domain (r_a in Figure 4c) was set to be 1.19 μm while the extension of the PMMA ring around it (r_b in Figure 4c) was set to be 0.22 μm, both values being averages calculated from the topographical/optical images shown in Figure 3. A condition of no flux was imposed at the cylindrical surface defined by $r = r_a + r_b$, in order to approximate the conditions of an infinite close-packed array of microelectrodes (*e.g.*, Figure 3e), as detailed in the Methods Section. Note that the simulation domain represented by Figure 4c is a simplified representation, but will give a good guide as to the general shape of a macroscopic CV curve.[54]

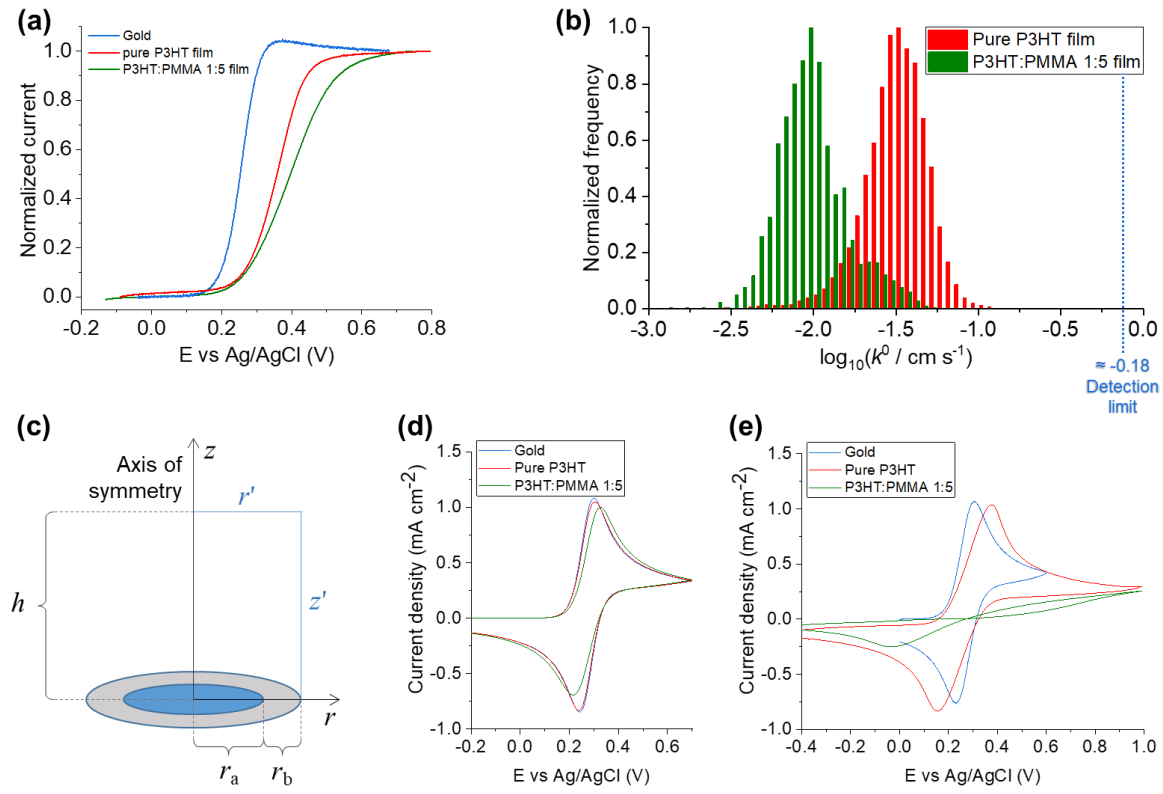

Figure 4. **(a)** Normalized near steady-state voltammograms (υ = 1 V s^{-1}) obtained from the FcDM$^{0/+}$ process in the SECCM configuration (probe diameter ≈ 200 nm) on Au, P3HT and 1:5 P3HT/PMMA blend electrodes. The curves were obtained by averaging 278, 9567 and 1826 individual measurements respectively on the Au, P3HT and P3HT domains of the 1:5 P3HT/PMMA blend electrode, respectively. **(b)** Histograms of measured k^0 values for P3HT and 1:5 P3HT/PMMA blend electrodes (logarithmic scale), with an indication of the maximum k^0 that can be calculated (limit of detection) with the employed method (dotted blue line). **(c)** Schematic of the 2D axisymmetric geometry built in COMSOL Multiphysics to represent the 1:5 P3HT/PMMA blend electrode. Boundaries r_a and r_b represent the active (conductive) P3HT and inactive (insulating) PMMA domains, respectively. r_a and r_b values of 1.19 µm and 0.22 µm, respectively, were determined with optical microscopy (see Figure 3c). **(d)** Simulated and **(e)** experimental macroscopic CVs (υ = 0.1 V s^{-1}). In (a), (b), (d) and (e), the blue, red and green curves refer to the Au, P3HT and 1:5 P3HT/PMMA blend electrodes, respectively. All experiments were performed with a 4.5 mM FcDM + 100 mM KCl solution.

Simulated cyclic voltammograms (CVs) obtained at a scan rate of 0.1 V s^{-1} are shown in Figure 4d. A relatively low mass-transport coefficient is obtained at this moderate scan rate, k_m ≈ 2 × 10^{-3} cm s^{-1} (estimated from the voltammetric peak current, calculation detailed in Supporting Information, Section S.4). In addition, a minimum diffusion layer thickness on the order of 40 µm ($\approx D/k_m$) is estimated, meaning the diffusion fields from the individual active

P3HT domains of the 1:5 P3HT:PMMA blend (≈2.3 μm in diameter and separated by ≈2.9 μm, see Figure 3a) overlaps fully on this timescale, and thus planar diffusion can be assumed (note that this has been incorporated into the model described by Figure 4c). Note that due to the relatively low k_m value, the macroscopic voltammetric response simulated for the pure P3HT film is indistinguishable from the Au electrode (*i.e.*, both are electrochemically reversible, compare red and blue curves), while the 1:5 P3HT:PMMA blend electrode shows a larger voltammetric peak-to-peak separation (ΔE_p = 118 mV, compared to 56 mV of the other two, reversible cases). In other words, despite the different properties of the three electrode materials, the simulations predict that macroscopic cyclic voltammetry can only distinguish between the pure P3HT and 1:5 P3HT:PMMA cases, but not the Au and the pure P3HT cases (electrochemically reversible). Thus, a major reason why conventional cyclic voltammetric methods of analysis alone are not suitable for benchmarking the quality of conductive polymer films as electron conductors (*i.e.*, electrodes) is susceptibility to ohmic resistance (*iR* drop), particularly at the high scan rates required to probe the kinetics of rapid electron-transfer processes (explored below). In addition, even if the complications from *iR* drop were to be avoided, in the absence of spatial-information on electrochemical reactivity (*i.e.*, obtained from SECCM mapping), a number of assumptions would need to be made (*i.e.*, uniform size, spacing and reactivity of the P3HT domains, see Figure 4c) to quantitatively interpret macroscopic electrochemical data, as in Figure 4d.

For comparison with the simulations, macroscopic cyclic voltammetry was carried out on an Au macrodisk electrode, a P3HT film electrode and a 1:5 P3HT:PMMA blend electrode, shown in Figure 4e. A full comparative study of the pure P3HT, 5:1, 1:1, and 1:5 P3HT:PMMA blends is given in the Supporting Information, Section S.6, as a function of scan rate. Evidently, while the experimentally measured CV on the Au macrodisk is in excellent agreement with theory (see Supporting Information, Figure S15a for direct comparison), the CVs obtained on

the pure P3HT and 1:5 P3HT:PMMA blend are vastly different to those predicted by simulation (Figure S15b and c, respectively). Both polymer electrodes exhibit dramatic shifts in peak potential (towards more positive and negative values for the oxidation and reduction peak, respectively) and decreases in the peak current density compared to the reversible case (Au). In particular, the 1:5 P3HT:PMMA blend does not exhibit classical peak shaped current-potential behavior during the forward potential scan, rather showing a flattened, plateau-type response that gives rise to a positive hysteresis on the reverse sweep. Naive interpretation of these data may indicate that the electrochemical activity of P3HT can be dramatically influenced by blending with PMMA, with the k^0 value associated with the $FcDM^{0/+}$ process decreasing by several orders of magnitude between pure P3HT electrode and the 1:5 P3HT:PMMA blend. However, when compared qualitatively across the four P3HT:PMMA ratios in the Supporting Information, Section S.6, it is rather apparent that the voltammetric peak potential separation correlates with the macroscopic conductivity, provided in Table S4.

As alluded to above, the large discrepancy between the experimental (Figure 4e) and simulated CVs predicted from analysis with SECCM (Figure 4d) is reasonably attributed to the presence of uncompensated resistance (R_u). For conventional metallic (conductor) electrodes, R_u is typically a small fraction of the solution resistance (R_s) arising from the finite separation between working and reference electrodes and is included in the measured potential as an ohmic drop term (iR_u). In the present case, it is assumed that an additional resistance arising from the finite electrical conductivity of the polymer films (as well as the P3HT-ITO interface), R_{film}, also contributes to R_u. Such resistive components can be considered to be in series, *i.e.*, their effect is summed. While R_s is constant in all experiments, R_{film} is a macroscopic property that depends on the composition of the polymer electrode, herein increasing with PMMA content in the blend. Therefore, simulations that incorporate R_u can emulate the general shape of the experimental CVs for the P3HT (R_u = 115 Ω, Supporting Information, Figure S16a) and

1:5 P3HT:PMMA blend ($R_u \approx 5000$ Ω, Figure S16b) electrodes. Note that in the simulations, R_u (and therefore R_{film}) is assumed to be independent of potential, which is likely to be an oversimplification, as P3HT is known to exhibit potential-dependent conductivity (*i.e.*, R_{film} is potential-dependent).[55] In any case, as R_u is the predominant factor controlling the potential-dependent electron transfer rate, the macroscopic CVs (Figure 4e) cannot be analyzed straightforwardly to reveal the structure-dependent k^0 values, as previous studies on similar materials would seem to suggest.[4, 56, 57]

As detailed above (and in SI, Section S.4), k_m value calculated for a fully active surface (*i.e.*, pure P3HT) at the macroscale ($\upsilon = 0.1$ V/s) is *ca.* 2×10^{-3} cm s^{-1}. When corrected for the fact that only ≈10% of the 1:5 P3HT:PMMA surface is active (from XPS and C-AFM), a k_m value of *ca.* 1×10^{-2} cm s^{-1} is calculated on the individual P3HT domains (UMEs), which is approximately 10% of that in the SECCM configuration ($k_m \approx 8 \times 10^{-2}$ cm s^{-1}, Section S.4). Based on this, in the absence of iR_u effects, one would expect that the macroscopic CV would be closer to reversible than that measured in the SECCM configuration, which, when comparing Figures 4a and 4e, is contrary to what is observed experimentally. Thus, the differences between the experimental and simulated macroscopic CVs in Figures 4d and 4e are solely attributable to iR_u (predominantly R_{film} in the case of the 1:5 P3HT:PMMA blend), and the SECCM-averaged CVs (Figure 4a) reflects the iR_u-free response of the P3HT domains. As explored in the Supporting Information, Section S.4 (Figure S9), while charge-transfer (*i.e.*, electron transport) within the P3HT domains is linear (planar) at the macroscale, the nanoscale droplet-cell configuration of SECCM is able to access additional lateral charge-transfer pathways within the film (*i.e.*, radial charge transport), decreasing the effective R_{film}. This, in addition to the small currents (*i.e.*, < 20 pA, herein) measured in SECCM renders this technique relatively immune to iR_u effects,[29] meaning that it can be applied to study the electrochemical

properties of relatively resistive materials such as conductive polymer blends (herein) and semiconductors.[33, 34]

Degradation of microscopic electrochemical properties due to sample aging. P3HT is known to undergo chemical degradation upon prolonged exposure (*i.e.*, on the days to weeks timescale) to ambient conditions (*i.e.*, light and atmospheric oxygen).[58, 59] The chemical degradation is expected to alter the electrochemical performance, as demonstrated from macroscale CVs on the pure material, shown in the Supporting Information, Section S.8. Briefly, any chemical reaction can degrade the film and alter the local density of states and thus the rate of electron transfer. Therefore, shown below, local electrochemical activity may serve as a far more sensitive probe to spatial degradation effects than what can currently be measured chemically.

The spatial instability of the polymer electrode was explored using voltammetric SECCM, employing the protocol outlined above to scan the 1:5 P3HT:PMMA blend electrode after "aging" under ambient conditions for a period of three weeks. Evident from the SECCM topography map in Figure 5a, the area scanned on the aged blend electrode is structurally analogous to that of the fresh electrode (see above, Figure 3d), with µm-sized islands of conductive P3HT within a matrix of insulating PMMA. However, when viewing the spatially-resolved current-potential data, shown in the Supporting Information, Movie S3, it clear that the "aged" blend electrode exhibits a significantly different pattern of nanoscale reactivity compared to the "fresh" electrode above. There are statistical differences between the current measured at the individual P3HT domains at the aged surface, with only a single domain attaining a mass-transport limited current for the $FcDM^{0/+}$ process within the examined potential window (–0.11 to 0.88 V vs Ag/AgCl), as shown in Figure 5b. This indicates that k^0 varies significantly from domain-to-domain (*i.e.*, orders-of-magnitude differences), which contrasts the fresh sample where all P3HT domains attained an identical mass-transport limited

current within the scanned potential window (Figure 3e) and relatively small inter-domain variations in k^0 were observed.

Figure 5c shows the averaged steady-state voltammograms extracted from individual P3HT domains. As noted above, only a single domain supported a mass-transport limited current, labelled **1** in Figure 5b and c, from which a k^0 value of *ca.* 5×10^{-3} cm s^{-1} was calculated, which is approximately half of that measured at the fresh electrode surface (*vide supra*). The absence of a mass-transport limited current plateau (within the investigated potential window) precludes quantitative analysis for the other domains, but it is clear that the k^0 value progressively decreases from curve **2** to **6**. The slowest response is barely distinguishable from the (stray) capacitive response obtained on the insulating PMMA areas (normalized to 0 in the plot). Evidently, exposure to the ambient atmosphere on the weeks timescale significantly affects the electron-transfer properties of P3HT, whether pure (Figure S17) or blended with PMMA (Movie S3 and Figure 3c).

While the chemical mechanism leading to these observed changes is beyond the scope of this proof-of-concept, it can be postulated that variations in the local chemical environment arising from differences in composition/structure (*i.e.*, PMMA content) or oxygen diffusion rates at the individual P3HT domain level could alter degradation rates at the (sub)microscale. Such non-uniform (spatially-dependent) degradation rates would be "invisible" in a conventional macroscopic CV, which is controlled by electrode-film resistance (*i.e.*, R_{film} contributing to R_u) rather than redox reactions (*i.e.*, the $FcDM^{0/+}$ process). SECCM clearly serves as a more sensitive screening tool for (electro)chemical degradation of semiconductor materials, with broader applicability beyond just organic electronics.

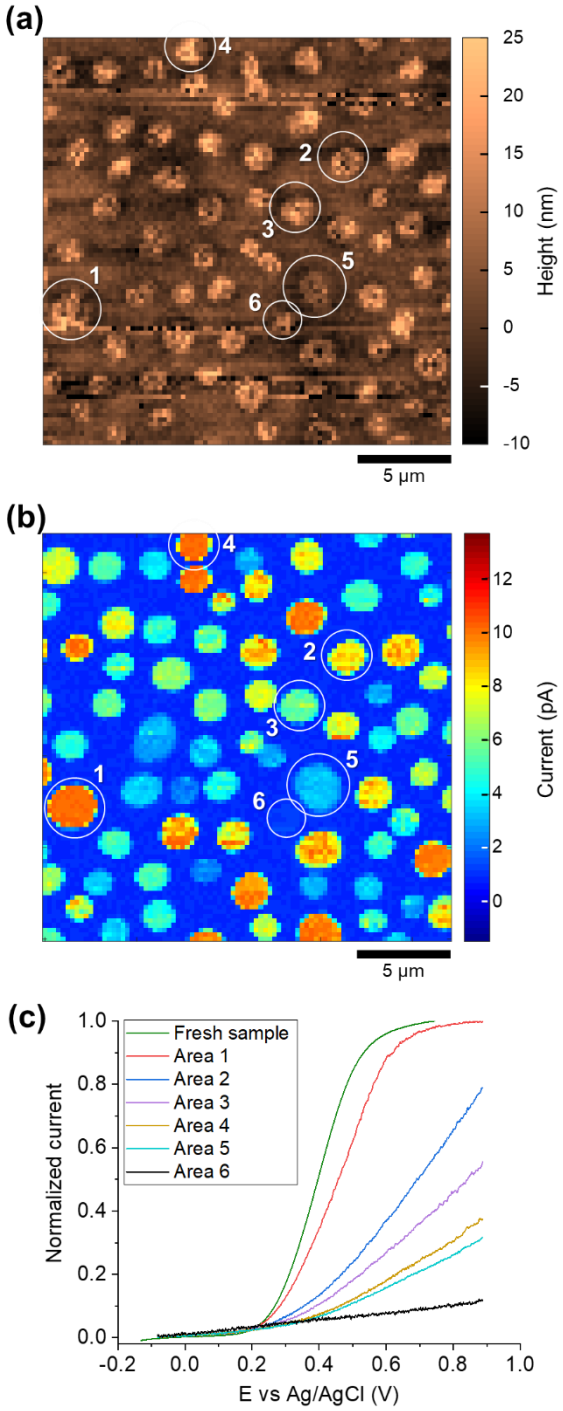

Figure 5. (a) Topographical and corresponding **(b)** electrochemical activity map recorded in the SECCM configuration (89 by 89 pixels, hopping distance = 0.25 µm, 2.38 s pixel^{-1}), visualizing the $FcDM^{0/+}$ process on an aged 1:5 P3HT:PMMA blend electrode. (b) is a single frame of Movie S3, taken at 0.88 V vs Ag/AgCl. **(c)** Normalized near steady-state voltammograms (υ = 1 V s^{-1}) extracted from the six P3HT domains labelled in (b), alongside that extracted from a fresh 1:5 P3HT:PMMA blend electrode (see Figure 2). The curves were obtained by averaging all "active" pixels within the individual P3HT domains. The nanopipet probe was ≈ 200 nm in diameter and contained 4.5 mM FcDM + 100 mM KCl.

CONCLUSIONS

This study advocates the use of *correlative electrochemical multi-microscopy* to understand the underlying structural factors governing electron-transfer in complex, structurally-heterogeneous electrode materials from the nanoscale to macroscale. Systematic investigation of pure P3HT and P3HT/PMMA blend electrodes with a suite of high-resolution microscopy/spectroscopy techniques (*e.g.*, c-AFM, SINS) revealed that the isolated domains of P3HT retain, mostly, bulk-like chemical and electronic structure when blended with PMMA, with the possibility of low concentration PMMA intercalation into the conductive polymer. Further correlation of these properties with quantitative, nanoscale resolution electrochemical flux movies from SECCM revealed only a slightly reduced electron-transfer rate constant (*i.e.*, k^0 value) for the $FcDM^{0/+}$ process in the isolated P3HT domains compared to pure P3HT electrodes at a commensurate length scale. Combining these data with complementary FEM simulations, macroscopic electrochemical behavior was predicted and further compared to experiment, demonstrating that electrode-film resistance, rather than redox reaction kinetics (*i.e.*, $FcDM^{0/+}$), controls the measured macroscopic electrochemistry of these polymer blend electrodes. These results suggest that conventional bulk voltammetric measurements should be used with caution to assess the quality of conductive polymers as electrodes. With this additional knowledge, the ambient exposure-induced degradation of P3HT/PMMA blend electrodes was interrogated with SECCM to reveal a spatially-heterogeneous loss of P3HT electroactivity, with individual P3HT domains affected to dramatically different extents. Overall, this study highlights the great strength of SECCM for resolving structure-property (*e.g.*, electrochemical activity or degradation) relationships in complex (electro)materials such as conductive polymer blends and for predicting the factors that control electrochemistry across length scales. This work further highlights the need for chemical analysis techniques that can be carried out at a commensurate scale to SECCM in order to aid rationalization and

interpretation of observed nanoscale electrochemical effects. The presented approaches should be generally applicable to any class of conductive polymer (or polymer blend), and offers the possibility for re-evaluating and optimizing materials that were previously discarded due to apparently poor macroscopic electrochemical properties.

METHODS

Details on the characterization techniques employed, nanopipet probes used in SECCM and further FEM simulations performed are provided in the Supporting Information, Section S.1.

Chemicals. Potassium chloride (KCl, Honeywell, 99.5%), 1,1′-ferrocenedimethanol (FcDM, Sigma-Aldrich, 97%), Triton X-100 (Sigma, laboratory grade), poly(3-hexylthiophene) (P3HT, Rieke, average molecular weight 57,000), poly(methyl methacrylate) (PMMA, Aldrich, average molecular weight 120,000) and 1,2-dichlorobenzene (Acros, 99%) were used as supplied by the manufacturer. All solutions were prepared with deionized water (resistivity = 18.2 MΩ.cm at 25°C).

Film preparation. Indium tin oxide (ITO)-coated glass substrates (Colorado Concept Coatings, sheet resistance < 15 ohm/square) were cleaned by Triton X-100 diluted with ultrapure water followed by successive sonication in 50:50 deionized water/ethanol, pure ethanol, pure acetone, and pure isopropanol and dried in a stream of nitrogen. Stock solutions of 13 mg/mL of poly(3-hexylthiophene) and poly(methyl methacrylate) were allowed to dissolve overnight in 1,2-dichlorobenzene on a hotplate at 80 °C under constant stirring. Stock solutions were mixed by volume to create, 5:1, 1:1 and 1:5 mixtures of P3HT to PMMA (wt %) and allowed to mix for 15 minutes before casting. Films were filtered using 0.45 μm PTFE filters (Fisherbrand) spin cast at 1000 rpm for 1 minute on Laurell spin coater (500 rpm for acceleration) and annealed at 120°C for 20 minutes. Conductivity measurements were

performed using the two-point probe method on interdigitated ITO substrates (Ossila) with channel dimensions of 30 mm width × 50 μm length.

Scanning electrochemical cell microscopy. All experiments in the SECCM configuration were carried out on a home-built scanning electrochemical probe microscopy (SEPM) workstation, as detailed in previous works.[27, 47] In brief, the SECCM platform used herein is comprised of *x*-*y*-*z* piezoelectric positioners (*z*: P-753.1CD; *xy*: P-733.2DD, from Physik Instrumente, Germany), a homebuilt bi-potentiostat with two current followers (electrometers), a waveform generator and a data collection system. The latter two are both integrated in an FPGA card, used respectively for applying potential to the system and recording the output from the custom electronic equipment.

During operation, the nanopipet probe equipped with Ag/AgCl QRCEs (detailed in the Supporting Information, Section S1) was mounted on the *z*-piezoelectric positioner and moved to the initial position using coarse *x*-*y*-*z* micropositioners (M-461-XYZ-M, Newport, U.S.A.). The ITO-supported polymeric film electrode was attached to an SEM pin stub with conductive silver paste, ensuring electrical contact. The stub was then positioned on a custom sample holder and placed on the *x*-*y* piezoelectric positioner. A scheme of the SECCM set up, during operation, is shown in Figure 6. The piezoelectric positioners and electrometers were placed in an aluminum faraday cage equipped with heat sinks and acoustic foam, which was situated on a passive pneumatic mechanical vibration isolator (S-2000A-423.5, Newport, U.S.A.). This configuration has previously been shown to minimize electric noise, thermal drift and mechanical vibration.[34, 60, 61] All input signals were measured every 4 μs and averaged 129 times, to give a data acquisition rate of 516 μs per point. Current signals were passed through a low-pass filter with a cut-off frequency of 1 kHz (time constant, t_c = 1 ms). All data acquisition and instrumental control was carried out with an FPGA card (PCIe-7852R) controlled by a LabVIEW 2016 (National Instruments, U.S.A.) interface running the Warwick

Electrochemical Scanning Probe Microscopy software (WEC-SPM, www.warwick.ac.uk/electrochemistry).

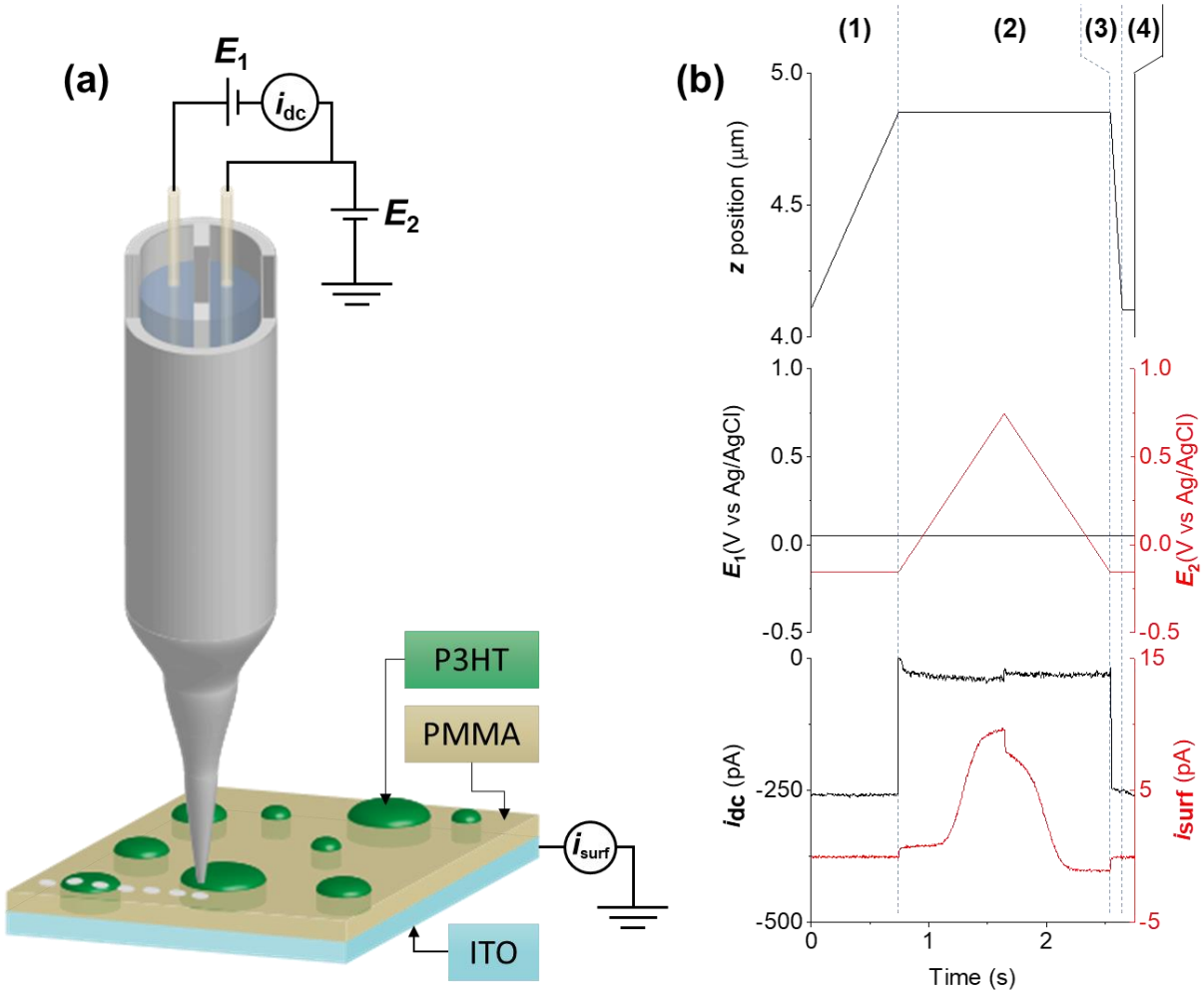

Figure 6. (a) Scheme of the voltammetric SECCM set up employed herein. During operation, a potential bias (E_1) was applied between identical Ag/AgCl QRCEs located in the two channels of the nanopipet probe, inducing a *dc* ion current (i_{dc}), which served as a feedback signal to detect meniscus-surface contact. A substrate voltage (E_2) was applied to one of the QRCEs to control the working electrode (*i.e.*, 1:5 P3HT:PMMA blend electrode shown) potential (E_s), where $E_s = -(0.5 \cdot E_1 + E_2)$, and the working electrode current (i_{surf}) was measured. The probe was translated across the substrate (working electrode) surface through the use of piezoelectric positioners in a "hopping mode" configuration. **(b)** Example plots of (i) *z*-position, (ii) E_1 and E_2, and (iii) i_{dc} and i_{surf} as a function of time, recorded simultaneously during a single approach to a P3HT domain within a 1:5 P3HT:PMMA blend electrode, with a nanopipet (diameter ≈ 200 nm) containing 4.5 mM FcDM + 100 mM KCl.

SECCM was carried out in the voltammetric hopping mode, as previously described.[41] This protocol involves approaching the probe to the surface of interest at a series of predefined grid

points, and carrying out a single electrochemical experiment (cyclic voltammetry, herein) on each landing. In this context, the term "landing" refers to droplet (meniscus) contact; the probe itself does not make physical contact with the surface. As noted above, a *dc* ion current (indicated by i_{dc} in Figure 6), induced by applying a bias of 50 mV (indicated by E_1 in Figure 6) between the QRCEs located in the two channels of the nanopipet probe, served as a feedback signal to detect each landing (*i.e.*, meniscus-surface contact), at which time the *z*-approach was halted. Cyclic voltammetry was performed by sweeping the potential of one of the QRCEs (indicated by E_2 in Figure 3), which controlled the substrate (working electrode) potential (E_{surf}), where $E_{surf} = -(0.5 \cdot E_1 + E_2)$, and the surface (working electrode) current (i_{surf}) was measured. Figure 6b shows representative examples of the *z*-extension, applied potentials (E_1, E_2) and the measured currents (i_{dc} and i_{surf}) for a single "hop" of a scanning experiment. During approach [Figure 6b, (1)], i_{dc} adopts a fixed value ("non-contact" value) which depends on the electrolyte composition, tip geometry and bias potential.[47] Landing is detected by a large spike (several hundreds of pA) in i_{dc} as the meniscus is deformed due to surface contact [Figure 6b, (2)], which serves as a feedback signal to halt the *z*-approach. Once on the surface [Figure 6b, (3)], the *z*-position is fixed, and cyclic voltammetry was performed by sweeping E_2, as i_{surf} is measured. After the measurement [Figure 6b, (4)], the probe is retracted and translated in x/y space, while i_{dc} returns to its non-contact value for the next "hop". Note that to accommodate for drift in i_{dc}, the feedback threshold was defined relative to the non-contact value on each and every hop in a self-referencing regime.[61, 62]

Note that the area of contact between the droplet and the surface, and therefore the active working electrode area, depends on the geometry of the probe and the characteristics of the electrolyte and the surface (*i.e.*, wettability of the surface). The usual method for determining the wetted area, *i.e.*, observing the droplet "footprints", that is the mark left on the surface due to surface modification or electrolyte residue, post-measurement using scanning electron

microscopy (SEM),[29] was not applicable in this case, due to the damage caused on the polymer surface by the electron beam. Thus, in order to determine the dimensions of the droplet cell, the constant-distance mode of SECCM was deployed, [27,28] measuring the footprint by translating the probe over the boundary separating a conductive P3HT domain from a non-conductive PMMA domain, as outlined in the Supporting Information, Section S.9. The wetted area was determined to be ≈ 1.5 times the diameter of the probe, consistent with previous studies in this configuration.[63]

After collection, all raw data were processed using the Matlab R2018b (Mathworks, U.S.A.) software suite. Non-linear sample tilt and drift in topographical maps were corrected using the scanning probe image processing (SPIP) software package (v. 6.0.14, Image Metrology, Denmark). The plotting of the data was performed with the OriginPro 2019 64bit (b9.3.226, OriginLab, U.S.A.) and Matlab R2018b (for the 2D maps) software packages. Note that all topographical and electrochemical maps were plotted without any data interpolation.

Finite element method (FEM) simulations. Finite element method (FEM) simulations were carried out in two different configurations, depending on the electrode system under configuration. (In all cases, a one electron electron-transfer reaction governed by the Butler-Volmer formalism of electrode kinetics was considered). The homogeneously active electrodes, that is the Au (*i.e.*, reversible case) and pure P3HT film electrodes were simulated using the DigiElch software package (v.8.FD, Gamry, U.S.A.), employing a planar geometry and semi-infinite one-dimensional (1D) diffusion regime. In the simulations, the bulk concentration of FcDM was set at 4.5 mM, E^0 was set to 0.271 V, the diffusion coefficient of $FcDM^0$ and $FcDM^+$ were set to 8×10^{-6} cm^2 s^{-1} and the electrode area was set at 0.021 and 0.55 cm^2 for the Au and P3HT electrode, respectively. The kinetic parameters, k^0 and α, were set to be 1 cm s^{-1}, 0.5 (electrochemically reversible) and 0.03 cm s^{-1} and 0.6 (measured

experimentally) for the Au and P3HT film electrodes, respectively. Note that unless explicitly stated, R_u was set to 0 Ω in all simulations.

In the case of the heterogeneously active 1:5 P3HT:PMMA blend electrode, FEM simulations were performed using the COMSOL Multiphysics software package (v.5.1, COMSOL Inc., Sweden). A bi-dimensional axisymmetric simulation set up was employed, using a rectangular cell with edges denoted *r* (bottom), *z* (left), *r*′ (top) and *z*′ (right), as shown in Figure 4c. The cell dimensions were set to 1.61 µm width (corresponding to $r_a + r_b$, see Figure 4c) and 500 µm height (corresponding to *h*), with *z* set as the symmetry axis. On both the left (*z*) and right (*z*′) edges, the condition of zero flux was imposed, as well as on the bottom edge (*r*) along r_b (*i.e.*, the insulating PMMA domain). On the top edge (*r*′), both zero flux and constant concentration conditions were imposed (with $C_{r'}$ = 4.5 mM). No concentration condition was imposed on *z*′. On the P3HT simulation domain (all over r_a), a potential-dependent flux, governed by Butler-Volmer electrode kinetics was employed, with k^0 and α set to 0.008 cm s^{-1} and 0.4 (measured experimentally). As above, the bulk concentrations of $FcDM^0$ and $FcDM^+$ were set to 4.5 and 0 mM, respectively.

ASSOCIATED CONTENT

Supporting Information. Extended experimental methods (Section S.1); additional polymer film characterization (S.2); movie captions (S.3); microscopic kinetic analysis with steady-state voltammetry, including additional FEM simulations (S.4); SECCM performed on pure P3HT and correlations between k^0/electrical conductivity and P3HT domain size (S.5); macroscopic electrochemistry and analysis carried out on all P3HT/PMMA blends (S.6); additional macroscopic simulations-experiment comparisons (S.7); degradation of the macroscopic electrochemical properties of P3HT upon ambient exposure (S.8) and; stability and wetting of the SECCM droplet cell (S.9). Spatially-resolved electrochemical flux movies visualizing the $FcDM^{0/+}$ process on pure P3HT (Movie S1), fresh 5:1 P3HT:PMMA (Movie S2) and degraded

(ambient-exposed) 5:1 P3HT:PMMA (Movie S3). The Supporting Information is available free of charge on the ACS Publications website at DOI: XXX.

AUTHOR INFORMATION

Corresponding Authors

*E-mail: C.Bentley.1@warwick.ac.uk (C.L.B.).
*E-mail: P.R.Unwin@warwick.ac.uk (P.R.U.).
*Email: ratcliff@email.arizona.edu (E.L.R.)

Author Contributions

The manuscript was written through contributions of all authors. All authors have given approval to the final version of the manuscript. ‡ E.D. and Z.C. contributed equally.

Funding Sources

A portion of this work is supported by the National Science Foundation under grant award DMR-1608289 (Z.C. and E.L.R). This research used resources of the Advanced Light Source, which is a DOE Office of Science User Facility under contract no. DE-AC02-05CH11231. SINS data was collected on beamline 5-4 under the assistance of Hans A. Bechtel. Use of the Stanford Synchrotron Radiation Lightsource, SLAC National Accelerator Laboratory, is supported by the U.S. Department of Energy, Office of Science, Office of Basic Energy Sciences under Contract No. DE-AC02-76SF00515. All Cypher AFM images and data were collected in the W.M. Keck Center for Nano-Scale Imaging in the Department of Chemistry and Biochemistry at the University of Arizona. The Cypher instrument purchase was supported by the National Science Foundation under Grant Number 1337371. FT-IR instrument purchase was supported by Arizona Technology and Research Initiative Fund (A.R.S.§15-1648). E.D. acknowledges Lubrizol Ltd. and the Warwick Collaborative Postgraduate Research Scheme for funding. C.L.B. acknowledges financial support from the Ramsay Memorial Fellowship

Trust. P.R.U. gratefully acknowledges support from a Royal Society Wolfson Research Merit Award.

References

1. Strakosas, X.; Bongo, M.; Owens, R. M., The Organic Electrochemical Transistor for Biological Applications. *J. Appl. Polym. Sci.* **2015,** *132*, 41735.

2. Rivnay, J.; Owens, R. M.; Malliaras, G. G., The Rise of Organic Bioelectronics. *Chem. Mater.* **2014,** *26*, 679-685.

3. Lin, P.; Yan, F., Organic Thin-Film Transistors for Chemical and Biological Sensing. *Adv. Mater.* **2012,** *24*, 34-51.

4. Wijeratne, K.; Ail, U.; Brooke, R.; Vagin, M.; Liu, X.; Fahlman, M.; Crispin, X., Bulk Electronic Transport Impacts on Electron Transfer at Conducting Polymer Electrode–Electrolyte Interfaces. *Proc. Natl. Acad. Sci.* **2018,** *115*, 11899-11904.

5. Mortimer, R. J.; Dyer, A. L.; Reynolds, J. R., Electrochromic Organic and Polymeric Materials for Display Applications. *Displays* **2006,** *27*, 2-18.

6. Lock, J. P.; Lutkenhaus, J. L.; Zacharia, N. S.; Im, S. G.; Hammond, P. T.; Gleason, K. K., Electrochemical Investigation of PEDOT Films Deposited via CVD for Electrochromic Applications. *Synth. Met.* **2007,** *157*, 894-898.

7. Arnold, S. P.; Harris, J. K.; Neelamraju, B.; Rudolph, M.; Ratcliff, E. L., Microstructure-Dependent Electrochemical Properties of Chemical-vapor Deposited Poly(3,4-Ethylenedioxythiophene) (PEDOT) Films. *Synth. Met.* **2019,** *253*, 26-33.

8. Liu, T.; Finn, L.; Yu, M.; Wang, H.; Zhai, T.; Lu, X.; Tong, Y.; Li, Y., Polyaniline and Polypyrrole Pseudocapacitor Electrodes with Excellent Cycling Stability. *Nano Lett.* **2014,** *14*, 2522-2527.

9. Zhang, Z.; Chen, X.; Chen, P.; Guan, G.; Qiu, L.; Lin, H.; Yang, Z.; Bai, W.; Luo, Y.; Peng, H., Integrated Polymer Solar Cell and Electrochemical Supercapacitor in a Flexible and Stable Fiber Format. *Adv. Mater.* **2014,** *26*, 466-470.

10. Janoschka, T.; Martin, N.; Martin, U.; Friebe, C.; Morgenstern, S.; Hiller, H.; Hager, M. D.; Schubert, U. S., An Aqueous, Polymer-Based Redox-Flow Battery Using Non-Corrosive, Safe, and Low-Cost Materials. *Nature* **2015,** *527*, 78-81.

11. Ratcliff, E. L.; Jenkins, J. L.; Nebesny, K.; Armstrong, N. R., Electrodeposited, "Textured" Poly(3-Hexyl-Thiophene) (e-P3HT) Films for Photovoltaic Applications. *Chem. Mater.* **2008,** *20*, 5796-5806.

12. Ratcliff, E. L.; Zacher, B.; Armstrong, N. R., Selective Interlayers and Contacts in Organic Photovoltaic Cells. *J. Phys. Chem. Lett.* **2011,** *2*, 1337-1350.

13. Bandodkar, A. J.; Jeerapan, I.; Wang, J., Wearable Chemical Sensors: Present Challenges and Future Prospects. *ACS Sens.* **2016,** *1*, 464-482.

14. Green, R. A.; Lovell, N. H.; Wallace, G. G.; Poole-Warren, L. A., Conducting Polymers for Neural Interfaces: Challenges in Developing an Effective Long-Term Implant. *Biomaterials* **2008,** *29*, 3393-3399.

15. Abidian, M. R.; Corey, J. M.; Kipke, D. R.; Martin, D. C., Conducting-Polymer Nanotubes Improve Electrical Properties, Mechanical Adhesion, Neural Attachment, and Neurite Outgrowth of Neural Electrodes. *Small* **2010,** *6*, 421-429.

16. Cui, X.; Lee, V. A.; Raphael, Y.; Wiler, J. A.; Hetke, J. F.; Anderson, D. J.; Martin, D. C., Surface Modification of Neural Recording Electrodes with Conducting Polymer/Biomolecule Blends. *J. Biomed. Mater. Res.* **2001,** *56*, 261-272.

17. Neelamraju, B.; Rudolph, M.; Ratcliff, E. L., Controlling the Kinetics of Charge Transfer at Conductive Polymer/Liquid Interfaces through Microstructure. *J. Phys. Chem. C* **2018,** *122*, 21210-21215.

18. Tsoi, W. C.; Spencer, S. J.; Yang, L.; Ballantyne, A. M.; Nicholson, P. G.; Turnbull, A.; Shard, A. G.; Murphy, C. E.; Bradley, D. D. C.; Nelson, J.; Kim, J.-S., Effect of Crystallization on the Electronic Energy Levels and Thin Film Morphology of P3HT:PCBM Blends. *Macromolecules* **2011,** *44*, 2944-2952.

19. Shallcross, R. C.; Stubhan, T.; Ratcliff, E. L.; Kahn, A.; Brabec, C. J.; Armstrong, N. R., Quantifying the Extent of Contact Doping at the Interface between High Work Function Electrical Contacts and Poly(3-Hexylthiophene) (P3HT). *J. Phys. Chem. Lett.* **2015,** *6*, 1303-1309.

20. Sirringhaus, H.; Brown, P. J.; Friend, R. H.; Nielsen, M. M.; Bechgaard, K.; Langeveld-Voss, B. M. W.; Spiering, A. J. H.; Janssen, R. A. J.; Meijer, E. W.; Herwig, P.; de Leeuw, D. M., Two-Dimensional Charge Transport in Self-Organized, High-Mobility Conjugated Polymers. *Nature* **1999,** *401*, 685-688.

21. Wang, X.; Lee, W. H.; Zhang, G.; Wang, X.; Kang, B.; Lu, H.; Qiu, L.; Cho, K., Self-Stratified Semiconductor/Dielectric Polymer Blends: Vertical Phase Separation for Facile Fabrication of Organic Transistors. *J. Mater. Chem. C* **2013,** *1*, 3989-3998.

22. Zhang, X.; Wang, B.; Huang, W.; Wang, G.; Zhu, W.; Wang, Z.; Zhang, W.; Facchetti, A.; Marks, T. J., Oxide-Polymer Heterojunction Diodes with a Nanoscopic Phase-Separated Insulating Layer. *Nano Lett.* **2019,** *19*, 471-476.

23. Bae, S.; Kim, H.; Lee, Y.; Xu, X.; Park, J.-S.; Zheng, Y.; Balakrishnan, J.; Lei, T.; Ri Kim, H.; Song, Y. I.; Kim, Y.-J.; Kim, K. S.; Özyilmaz, B.; Ahn, J.-H.; Hong, B. H.; Iijima, S., Roll-to-Roll Production of 30-Inch Graphene Films for Transparent Electrodes. *Nat. Nanotechnol.* **2010,** *5*, 574-578.

24. Wu, M.-C.; Liao, H.-C.; Lo, H.-H.; Chen, S.; Lin, Y.-Y.; Yen, W.-C.; Zeng, T.-W.; Chen, C.-W.; Chen, Y.-F.; Su, W.-F., Nanostructured Polymer Blends (P3HT/PMMA):

Inorganic Titania Hybrid Photovoltaic Devices. *Sol. Energy Mater. Sol. Cells* **2009,** *93*, 961-965.

25. Kergoat, L.; Battaglini, N.; Miozzo, L.; Piro, B.; Pham, M.-C.; Yassar, A.; Horowitz, G., Use of Poly(3-Hexylthiophene)/Poly(Methyl Methacrylate) (P3HT/PMMA) Blends to Improve the Performance of Water-Gated Organic Field-Effect Transistors. *Org. Electron.* **2011,** *12*, 1253-1257.

26. Janasz, L.; Marszalek, T.; Zajaczkowski, W.; Borkowski, M.; Goldeman, W.; Kiersnowski, A.; Chlebosz, D.; Rogowski, J.; Blom, P.; Ulanski, J.; Pisula, W., Ultrathin Film Heterojunctions by Combining Solution Processing and Sublimation for Ambipolar Organic Field-Effect Transistors. *J. Mater. Chem. C* **2018,** *6*, 7830-7838.

27. Ebejer, N.; Güell, A. G.; Lai, S. C. S.; McKelvey, K.; Snowden, M. E.; Unwin, P. R., Scanning Electrochemical Cell Microscopy: A Versatile Technique for Nanoscale Electrochemistry and Functional Imaging. *Annu. Rev. Anal. Chem.* **2013,** *6*, 329-351.

28. Bentley, C. L.; Kang, M.; Unwin, P. R., Scanning Electrochemical Cell Microscopy: New Perspectives on Electrode Processes in Action. *Curr. Opin. Electrochem.* **2017,** *6*, 23-30.

29. Bentley, C. L.; Edmondson, J.; Meloni, G. N.; Perry, D.; Shkirskiy, V.; Unwin, P. R., Nanoscale Electrochemical Mapping. *Anal. Chem.* **2019,** *91*, 84-108.

30. Bentley, C. L.; Kang, M.; Unwin, P. R., Nanoscale Surface Structure–Activity in Electrochemistry and Electrocatalysis. *J. Am. Chem. Soc.* **2019,** *141*, 2179-2193.

31. Unwin, P. R.; Guell, A. G.; Zhang, G., Nanoscale Electrochemistry of sp(2) Carbon Materials: from Graphite and Graphene to Carbon Nanotubes. *Acc. Chem. Res.* **2016,** *49*, 2041-2048.

32. Tao, B.; Yule, L. C.; Daviddi, E.; Bentley, C. L.; Unwin, P. R., Correlative Electrochemical Microscopy of Li-Ion (De)intercalation at a Series of Individual $LiMn_2O_4$ Particles. *Angew. Chem., Int. Ed.* **2019,** 58, 4606-4611.

33. Bentley, C. L.; Kang, M.; Maddar, F.; Li, F.; Walker, M.; Zhang, J.; Unwin, P. R., Electrochemical Maps and Movies of the Hydrogen Evolution Reaction on Natural Crystals of Molybdenite (MoS_2): Basal vs. Edge Plane Activity. *Chem. Sci.* **2017**, *8*, 6583-6593.

34. Bentley, C. L.; Kang, M.; Unwin, P. R., Nanoscale Structure Dynamics within Electrocatalytic Materials. *J. Am. Chem. Soc.* **2017,** *139*, 16813-16821.

35. Hill, J. W.; Hill, C. M., Directly Mapping Photoelectrochemical Behavior within Individual Transition Metal Dichalcogenide Nanosheets. *Nano Lett.* **2019**, *19*, 5710-5716.

36. Bentley, C. L.; Andronescu, C.; Smialkowski, M.; Kang, M.; Tarnev, T.; Marler, B.; Unwin, P. R.; Apfel, U.-P.; Schuhmann, W., Local Surface Structure and Composition Control the Hydrogen Evolution Reaction on Iron Nickel Sulfides. *Angew. Chem., Int. Ed.* **2018,** *57*, 4093-4097.

37. Chen, C.-H.; Meadows, K. E.; Cuharuc, A.; Lai, S. C. S.; Unwin, P. R., High Resolution Mapping of Oxygen Reduction Reaction Kinetics at Polycrystalline Platinum Electrodes. *Phys. Chem. Chem. Phys.* **2014,** *16*, 18545-18552.

38. Wang, Y.; Gordon, E.; Ren, H., Mapping the Nucleation of H_2 Bubbles on Polycrystalline Pt via Scanning Electrochemical Cell Microscopy. *J. Phys. Chem. Lett.* **2019,** *10*, 3887-3892.

39. Mariano, R. G.; McKelvey, K.; White, H. S.; Kanan, M. W., Selective Increase in CO_2 Electroreduction Activity at Grain-Boundary Surface Terminations. *Science* **2017,** *358*, 1187-1192.

40. Yule, L. C.; Bentley, C. L.; West, G.; Shollock, B. A.; Unwin, P. R., Scanning Electrochemical Cell Microscopy: a Versatile Method for highly Localised Corrosion Related Measurements on Metal Surfaces. *Electrochim. Acta* **2019,** *298*, 80-88.

41. Chen, C.-H.; Jacobse, L.; McKelvey, K.; Lai, S. C. S.; Koper, M. T. M.; Unwin, P. R., Voltammetric Scanning Electrochemical Cell Microscopy: Dynamic Imaging of Hydrazine Electro-Oxidation on Platinum Electrodes. *Anal. Chem.* **2015,** *87*, 5782-5789.

42. Daviddi, E.; Gonos, K. L.; Colburn, A. W.; Bentley, C. L.; Unwin, P. R., Scanning Electrochemical Cell Microscopy (SECCM) Chronopotentiometry: Development and Applications in Electroanalysis and Electrocatalysis. *Anal. Chem.* **2019,** *91*, 9229-9237.

43. Bentley, C. L.; Perry, D.; Unwin, P. R., Stability and Placement of Ag/AgCl Quasi-Reference Counter Electrodes in Confined Electrochemical Cells. *Anal. Chem.* **2018,** *90*, 7700-7707.

44. Ebejer, N.; Schnippering, M.; Colburn, A. W.; Edwards, M. A.; Unwin, P. R., Localized High Resolution Electrochemistry and Multifunctional Imaging: Scanning Electrochemical Cell Microscopy. *Anal. Chem.* **2010,** *82*, 9141-9145.

45. Sun, P.; Mirkin, M. V., Kinetics of Electron-Transfer Reactions at Nanoelectrodes. *Anal. Chem.* **2006,** *78*, 6526-6534.

46. Momotenko, D.; Byers, J. C.; McKelvey, K.; Kang, M.; Unwin, P. R., High-Speed Electrochemical Imaging. *ACS Nano* **2015,** *9*, 8942-8952.

47. Snowden, M. E.; Güell, A. G.; Lai, S. C. S.; McKelvey, K.; Ebejer, N.; O'Connell, M. A.; Colburn, A. W.; Unwin, P. R., Scanning Electrochemical Cell Microscopy: Theory and Experiment for Quantitative High Resolution Spatially-Resolved Voltammetry and Simultaneous Ion-Conductance Measurements. *Anal. Chem.* **2012,** *84*, 2483-2491.

48. Mirkin, M. V.; Bard, A. J., Simple Analysis of Quasi-Reversible Steady-State Voltammograms. *Anal. Chem.* **1992,** *64*, 2293-2302.

49. Rudolph, M.; Ratcliff, E. L., Normal and Inverted Regimes of Charge Transfer Controlled by Density of States at Polymer Electrodes. *Nat. Commun.* **2017,** *8*, 1048.

50. Reid, O. G.; Munechika, K.; Ginger, D. S., Space Charge Limited Current Measurements on Conjugated Polymer Films using Conductive Atomic Force Microscopy. *Nano Lett.* **2008,** *8*, 1602-1609.

51. Muller, E. A.; Pollard, B.; Bechtel, H. A.; van Blerkom, P.; Raschke, M. B., Infrared Vibrational Nanocrystallography and Nanoimaging. *Sci. Adv.* **2016,** *2*, e1601006.

52. Bard, A. J.; Faulkner, L. R., *Electrochemical Methods : Fundamentals and Applications*. 2nd ed.; Wiley: New York, 2001; p 833.

53. Marcus, R. A.; Sutin, N., Electron Transfers in Chemistry and Biology. *Biochim. Biophys. Acta, Rev. Bioenerg.* **1985,** *811*, 265-322.

54. Davies, T. J.; Ward-Jones, S.; Banks, C. E.; del Campo, J.; Mas, R.; Muñoz, F. X.; Compton, R. G., The Cyclic and Linear Sweep Voltammetry of Regular Arrays of Microdisc Electrodes: Fitting of Experimental Data. *J. Electroanal. Chem.* **2005,** *585*, 51-62.

55. Harris, J. K.; Neelamraju, B.; Ratcliff, E. L., Intersystem Sub-Population Charge Transfer and Conformational Relaxation Preceding in Situ Conductivity in Electrochemically Doped Poly(3-Hexylthiophene) (P3HT) Electrodes. *Chem. Mater.* **2019**, *31*, 6870-6879.

56. Milner, D. F.; Weaver, M. J., The Influence of Uncompensated Solution Resistance on the Determination of Standard Electrochemical Rate Constants by Cyclic Voltammetry, and some Comparisons with A.C. Voltammetry. *Anal. Chim. Acta* **1987,** *198*, 245-257.

57. Gennett, T.; Weaver, M. J., Reliability of Standard Rate Constants for Rapid Electrochemical Reactions. *Anal. Chem.* **1984,** *56*, 1444-1448.

58. Schafferhans, J.; Baumann, A.; Deibel, C.; Dyakonov, V., Trap Distribution and the Impact of Oxygen-Induced Traps on the Charge Transport in Poly(3-Hexylthiophene). *Appl. Phys. Lett.* **2008,** *93*, 093303.

59. Rivaton, A.; Chambon, S.; Manceau, M.; Gardette, J.-L.; Lemaître, N.; Guillerez, S., Light-Induced Degradation of the Active Layer of Polymer-Based Solar Cells. *Polym. Degrad. Stab.* **2010,** *95*, 278-284.

60. Kang, M.; Perry, D.; Bentley, C. L.; West, G.; Page, A.; Unwin, P. R., Simultaneous Topography and Reaction Flux Mapping at and around Electrocatalytic Nanoparticles. *ACS Nano* **2017,** *11*, 9525-9535.

61. Bentley, C. L.; Unwin, P. R., Nanoscale Electrochemical Movies and Synchronous Topographical Mapping of Electrocatalytic Materials. *Faraday Discuss.* **2018,** *210*, 365-379.

62. Page, A.; Perry, D.; Young, P.; Mitchell, D.; Frenguelli, B. G.; Unwin, P. R., Fast Nanoscale Surface Charge Mapping with Pulsed-Potential Scanning Ion Conductance Microscopy. *Anal. Chem.* **2016,** *88*, 10854-10859.

63. Guell, A. G.; Meadows, K. E.; Dudin, P. V.; Ebejer, N.; Macpherson, J. V.; Unwin, P. R., Mapping nanoscale Electrochemistry of Individual Single-Walled Carbon Nanotubes. *Nano Lett.* **2014,** *14*, 220-224.

For T.O.C. only

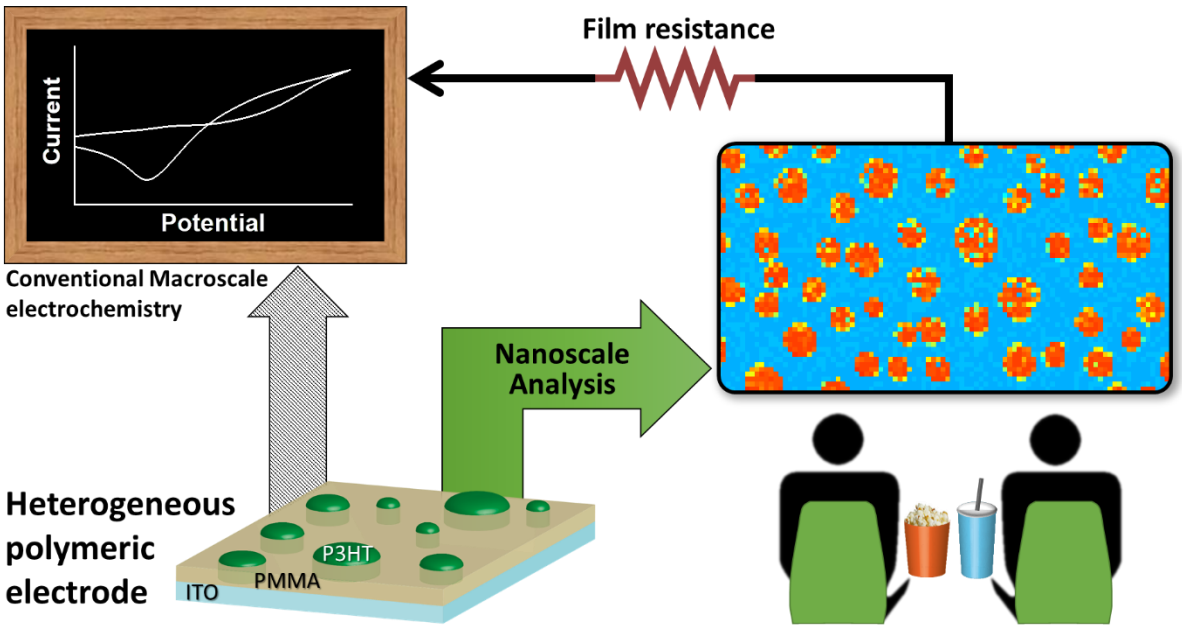
Film resistance
Current
Potential
Conventional Macroscale electrochemistry
Nanoscale Analysis
Heterogeneous polymeric electrode
P3HT
PMMA
ITO